Computer simulation of three dimensional shearing of granular materials. Formation of shear bands

Sándor Fazekas
Theoretical Solid State Research Group of the Hungarian Academy of Sciences
János Török
Department of Chemical Information Technology, BUTE, Hungary
János Kertész
Department of Theoretical Physics, BUTE, Hungary
Dietrich E. Wolf
Department of Physics, University Duisburg-Essen, Germany

ABSTRACT: We used computer simulations to study spontaneous strain localization in granular materials, as a result of symmetry breaking non-homogeneous deformations. Axisymmetric triaxial shear tests were simulated by means of standard three-dimensional Distinct Element Method (DEM) with spherical grains. Carefully prepared dense specimens were compressed between two platens and, in order to mimic the experimental conditions, stress controlled, (initially) axisymmetric boundary conditions were constructed. Strain localization gave rise to visible shear bands, previously found experimentally under similar conditions by several groups, and different morphologies could be reproduced. We examined the stress-strain relation during the process and found good agreement with experiments. Formation mechanism of shear bands is discussed.

1 INTRODUCTION

Spontaneous symmetry breaking in granular materials occurs in many different forms. Here we focus on strain localization and subsequent development of shear bands. Shear bands appear nearly always if dry granular material is subjected to shear. Its first study dates back to the nineteenth century and since then it was investigated in many different geometries and specially designed laboratory tests (e.g. plane strain, biaxial, and triaxial tests). Here we present numerical studies of axisymmetric triaxial tests, the most common laboratory tests in Geomechanics.

In a simplified picture, a triaxial test typically consists of a cylindrical specimen enclosed between two end platens and surrounded by a rubber membrane. An external pressure is applied on the membrane, either by placing the system into a pressurized fluid, or creating a relative vacuum inside the system. The end platens are pressed against each other in a controlled way, either with constant velocity (strain control) or with constant force (stress control). The force resulting on the platens, or the displacement rate of the platens is recorded, as well as the volume change of the specimen.

The triaxial test is an elementary test, performed to obtain mechanical properties of soils. Antifriction devices (lubricated end platens) were designed in order to suppress strong heterogeneous responses, such as barreling and localization of deformation along failure planes. In the past 20 years the study of localization patterns gained more attention and strain localization became an important research field, as experimental tools as Computed Tomography (CT) became available to study the internal structure of strained specimens (Desrues et al. 1996; Batiste et al. 2004). Such studies revealed complex localization patterns and shear band morphologies depending on the test conditions.

2 SIMULATION METHOD

We used standard three-dimensional Distinct Element Method (Cundall & Strack 1979) (also known as Molecular Dynamics) to perform simulations of strain controlled triaxial shear tests. As an advantage, contrary to the Finite Element Method (FEM) commonly used in sim-
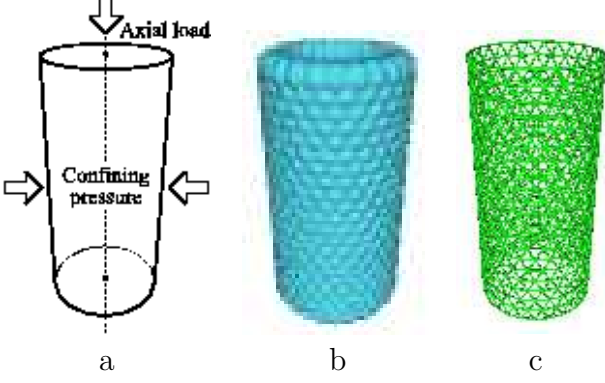
Figure 1. Simulation setup. A cylindrical specimen placed between rigid horizontal platens and surrounded by an elastic membrane is subjected to axial load and confining pressure.

ulations of soils, the Distinct Element Method (DEM) does not require any macroscopic *constitutive model*, instead it is based on a microscopic *contact model* (for a review see (Luding 2004) and references therein). We used the Hertz contact model (Landau & Lifshitz 1970) with appropriate damping (Brilliantov et al. 1996), combined with a frictional spring-dashpot model (Luding 2004).

The simulation setup can be seen on Fig. 1. An initially axisymmetric system of spherical grains (particles) was placed between two horizontal platens. The bottom platen was fixed. On the upper platen, having mass $M = 10^{-3}$ kg, an axial load was applied (as described later). The upper platen could not rotate along the vertical axis. The rotational inertia of the upper platen in tilting was $I = 10^{-7}$ kg m^2. The particles were surrounded by an "elastic membrane" composed of overlapping spheres having equal diameter $d_m = 10^{-3}$ m and mass density $\rho_m = 0.1 \cdot 10^3$ kg/m^3, and initially forming a triangular lattice (see part (b) of Fig. 1). The rotational degree of freedom of the "membrane nodes" was frozen (i.e. they could not rotate).

The "membrane nodes" were interconnected with linear springs having zero base length and initial elongation $l_0 = 0.5 \cdot 10^{-3}$ m (equal to the initial distance of neighboring "membrane nodes"). The force F_s, acting between two "membrane nodes" connected with a spring, was calculated as

$$F_s = \kappa_s l_s - \gamma_s v_s, \qquad (1)$$

where $\kappa_s = 0.5$ N/m and $\gamma_s = 10^{-3}$ N s/m are stiffness and damping coefficients, l_s is the spring's elongation and v_s is the relative velocity of the nodes. At any time the spring's elongation is equal to the relative distance of the nodes. The stiffness of the springs was chosen such that the particles could not escape by passing through the membrane. Additionally a confining pressure $\sigma_c = 0.5 \cdot 10^3$ N/m^2 was applied on the membrane, by calculating the forces acting on the triangular

facets formed by neighboring "membrane nodes" (see part (c) of Fig. 1). The effective external pressure in this setup is larger than σ_c, because the "membrane springs" have their own contribution as well, however, with the used parameters, this contribution is small compared to σ_c.

For simplicity we made no difference between particle-particle, particle-platen, and particle-membrane contacts. The normal F_n and tangential $\mathbf{F}_t$ components of the contact force were calculated as

$$F_n = \kappa_n \delta_n^{3/2} - \gamma_n \delta_n^{1/2} v_n, \qquad (2)$$
$$\mathbf{F}_t = \kappa_t \boldsymbol{\delta}_t - \gamma_t \mathbf{v}_t, \qquad (3)$$

where $\kappa_n = 10^6$ $N/m^{3/2}$, $\kappa_t = 10^4$ N/m, $\gamma_n = 1$ N $s/m^{3/2}$, and $\gamma_t = 1$ N s/m are the normal and tangential stiffness and damping coefficients, δ_n and $\boldsymbol{\delta}_t$ are normal and tangential displacements, and v_n and $\mathbf{v}_t$ are the normal and tangential relative velocities. The normal displacement δ_n, the normal velocity v_n, and the normal force F_n are one-dimensional quantities measured along to the normal vector of the contact plane, while the tangential displacement $\boldsymbol{\delta}_t$, the tangential velocity $\mathbf{v}_t$, and the tangential force $\mathbf{F}_t$ are two-dimensional vectors embedded in the contact plane.

Knowing the relative position, the shape, and the size of the bodies in contact, the normal displacement can be calculated directly. Calculating the tangential displacement is much more complicated: The tangential velocity must be integrated during the lifetime of the contact. This integration must be performed in the contact plane. In our simulation program the tangential displacement $\boldsymbol{\delta}_t$ was implemented as a 3D vector in the observational space. During integration, this vector was rotated as the local configuration changed, keeping it always in the contact plane.

The Coulomb friction law limits the frictional force to μF_n, where $\mu = 0.5$ is the coefficient of friction. To allow for sliding contacts, we also limited the length of the tangential displacement to $\mu F_n / \kappa_t$, shortening the displacement vector accordingly. This frictional spring-dashpot model implements both sliding and static friction.

Our simulations are run at zero gravity. After calculating the interaction forces, and adding the external load and confining pressure, the motion of bodies (grains, "membrane nodes", and upper platen) is calculated by solving numerically the Newton equations using a given $\Delta t = 10^{-6}$ s integration time step. The translational motion is calculated with Verlet's leap-frog method. The rotational state of bodies (given in quaternion representation) is integrated with Euler's method.

2

Table 1. Simulation runs.

	Upper platen velocity	Upper platen tilting
(a)	Base	Enabled
(b)	Base	Disabled
(c)	Two times faster	Enabled
(d)	Two times faster	Disabled

In quasi-static processes as the one simulated by us, the vibration introduced by grain (spring) elasticity is basically undesired noise. We checked the noise level in our simulations and set the parameters to keep it low. The inverse of the eigenfrequency of all contacts, in both normal and tangential direction, is more than one order of magnitude larger than the integration time step.

In the first part of the simulation (preparation phase) a hard cylinder touching the internal side of the membrane was introduced, and thus the membrane was neglected. The particle system was built by randomly placing spheres into this cylinder. The maximum allowed initial grain overlap was 1%. To assure reasonable execution time, we started with a sufficiently tall system (usually 3 time taller than the final system size). The particles (grains) were given equal mass density $\rho_p = 7.5 \cdot 10^3 \ kg/m^3$. The diameter of the spherical grains was taken from a Gaussian distribution with mean value $\langle d \rangle = 0.9 \cdot 10^{-3} \ m$ and standard deviation $\Delta d = 0.025 \cdot 10^{-3} \ m$, and cut at $4\Delta d$ around the mean value.

In the preparation phase the rotational degree of freedom of the upper platen was frozen and the coefficient of friction was set to zero. Each particle and the upper platen were given a velocity proportional to a contraction velocity $v_c = 80 \cdot 10^{-2} \ m/s$ and their distance from the bottom. The system contracted until the upper platen's velocity in grain-platen collisions decreased to zero. At this point an axial load $F_0 = 200 \cdot 10^{-3} \ N$ was switched on, which further contracted the system. After the system relaxed, the cylinder was removed, letting the membrane and the confining pressure carry the load. The axial load F_0 and the confining pressure σ_c were chosen such that the system came to equilibrium without barreling. We prepared one sample having diameter $D = 22 \cdot 10^{-3} \ m$ and height $H = 46 \cdot 10^{-3} \ m$, containing $N_p = 27000$ particles and $N_m = 14904$ membrane nodes. The sample's geometry factor $H/D \approx 2$, is similar to the typical geometry factors used in experiments.

For preparing sphere packings (Weitz 2004) many different methods exist (e.g. (Lubachevsky & Stillinger 1990; Sherwood 1997)). Using the deposition method described above, the volume fraction at the end of the preparation phase was $f_0 = 0.643$, which
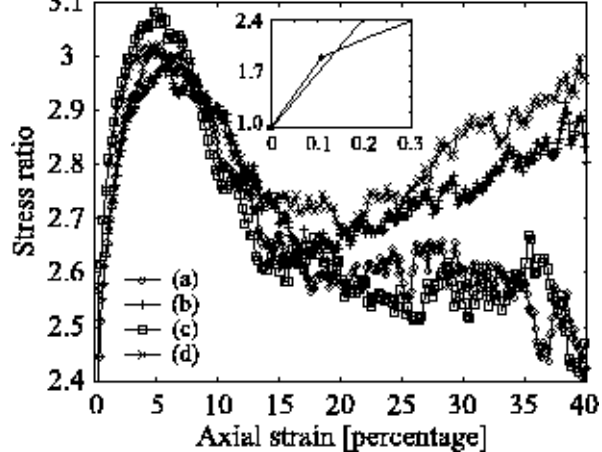

Figure 2. Stress-strain relation. The stress ratio (σ/σ_0, where σ_0 denotes the initial stress) measured on the upper platen is shown as function of the axial strain, for the executed simulation runs (see Tab. 1). (See inset for low stress ratios.) For the lower two curves (a, c) tilting of the upper plate was enabled, and for the upper two (b, d) it was disabled.

is slightly larger than the random close packing value of identical spheres, as expected for an ensemble of spheres with size dispersion.

After the preparation phase the sample was compressed by moving the upper platen downward in vertical direction with constant velocity u_c (strain controlled experiment). In the executed simulation runs we used two different velocities: $u_c = u_0 = 10^{-2} \ m/s$ (base value), and $u_c = 2u_0$ (two times faster). During compression, tilting of the upper platen was either enabled or disabled. We executed four different runs (see Tab. 1) starting from the same initial condition.

During the runs we measured the stress σ on the upper platen, and calculated the stress ratio σ/σ_0, where σ_0 denotes the initial stress. The identification of the shear bands is a non-trivial task. One possibility is to generalize the method used in two dimensions (Daudon et al. 1997), i.e., to calculate the shear intensity around the particles from the local deformation tensor. After doing this, we have realized that monitoring the rotational state of the particles is sufficient for the purpose of shear band identificiation, and it leads to the same results. Our observations are presented in the next section.

3 SIMULATION RESULTS

As the axial strain increases, the response of the granular sample (the stress ratio) increases until it reaches a peak value (see Fig. 2). This is a basic observation of triaxial shear tests of dense granular specimens (Lade 2002). Strain localization in granular materials is followed by a decrease in load bearing capacity. Dense granular materials dilate during shear. Due to this, the load bearing particle chains collapse. Shear bands occur after peak
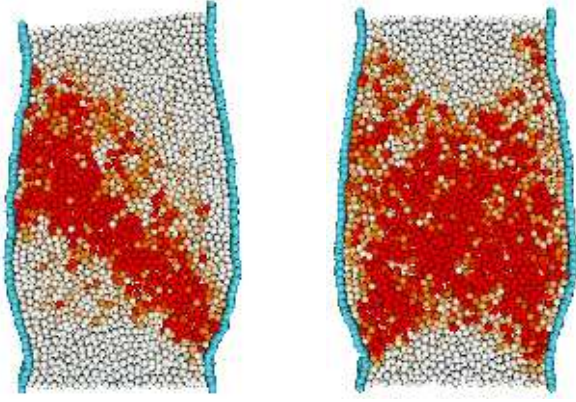
Figure 3. Vertical cross sections. The snapshots were taken at the middle of the sample at 10% axial strain from the (c) (left) and the (d) (right) simulations. The darkness (red content of color) is proportional to the rotational energy.

failure and result in further decrease in strength.

According to Fig. 2, up to 15% axial strain there is no significant difference in the stress-strain relation measured in the different simulation runs, indifferent of the strain rate and tilting of the upper platen. However, we observe a change after this point. At large axial strain values, when tilting of the upper platen was disabled, the stress ratio increases again.

Taking cross sections of the sheared samples, and coloring the grains according to their rotational state we could visualize the shear bands (see Fig. 3). On these renderings the larger the rotational energy, the more red (or darker in black-and-white version) a particle gets. The fact that the rotational state of the grains identifies the shear bands, is due to the fact that the shear bands are characterized not only by dilation but also by rotation of the grains, which is known from both experiments and simulations (Oda & Kazama 1998; Herrmann et al. 2004).

Another important result is that internal instabilities can develop into a symmetry-breaking localized deformation along a failure plane when tilting of the upper platen is enabled, while nontilting platens act as a stabilizing factor resulting in two axisymmetric conical surfaces and complex localization patterns around them (Fazekas et al. 2005). This result is confirmed by similar experiments executed in micro-gravity (Batiste et al. 2004), and proves that in the absence of reinforced axisymmetry, spontaneous symmetry breaking can take place as a result of internal instabilities (Desrues et al. 1996).

4 CONCLUSIONS

We executed triaxial shear test simulations using DEM. Different shear band morphologies known from experiments could be reproduced. To our knowledge it is the first time that these localization patterns were reproduced in DEM simulations. We showed that the shear bands can be identified with the rotational state of the grains, and symmetry breaking strain localization can develop if the symmetry is not enforced with nontilting platens. The agreement of our results with the experimental results is very good, even if the system size (number of particles) in our simulations is much smaller than in experiments.

REFERENCES

Batiste, S. N., Alshibli, K. A., Sture, S., & Lankton, M. 2004. Shear band characterization of triaxial sand specimens using computed tomography. *Geotechnical Testing Journal* 27: 568–579.

Brilliantov, N. V., Spahn, F., Hertzsch, J.-M., & Pöschel, T. 1996. Model for collisions in granular gases. *Phys. Rev. E* 53: 5382.

Cundall, P. A. & Strack, O. D. L. 1979. A discrete numerical model for granular assemblies. *Geotechnique* 29: 47.

Daudon, D., Lanier, J., & Jean, M. 1997. A micro mechanical comparison between experimental results and numerical simulation of a biaxial test on 2d granular material. In Behringer & Jenkins (eds), *Powders and Grains 1997*: 219–222. Balkema.

Desrues, J., Chambon, R., Mokni, M., & Mazerolle, F. 1996. Void ratio evolution inside shear bands in triaxial sand specimens studied by computed tomography. *Géotechnique* 46: 529–546.

Fazekas, S., Török, J., Kertész, J., & Wolf, D. E. 2005. (to be published).

Herrmann, H. J., Astrom, J. A., & Baram, R. M. 2004. Rotations in shear bands and polydisperse packings. *Physica A* 344: 516–522.

Lade, P. V. 2002. Instability, shear banding, and failure in granular materials. *International Journal of Solids and Structures* 39: 3337–3357.

Landau, L. D. & Lifshitz, E. M. 1970. *Theory of Elasticity*: Chapter 9. Pergamon, New York. (2nd English ed.).

Lubachevsky, B. D. & Stillinger, F. H. 1990. Geometric properties of random disk packings. *J. Stat. Phys.* 60: 561–583.

Luding, S. 2004. Molecular dynamics simulations of granular materials. In H. Hinrichsen & D. E. Wolf (eds), *The Physics of Granular Media*. Wiley-VCH.

Oda, M. & Kazama, H. 1998. Microstructure of shear bands and its relation to the mechanisms of dilatancy and failure of dense granular soils. *Geotechnique* 48: 465–481.

Sherwood, J. D. 1997. Packing of spheroids in three-dimensional space by random sequential add. *J. Phys. A: Math. Gen.* 30: L839–L843.

Weitz, D. A. 2004. Packing in the spheres. *Science* 303: 968–969.